The Astrophysical Journal, 983:7 (15pp), 2025 April 10 https://doi.org/10.3847/1538-4357/adbae9

Limited Hysteresis in the Atmospheric Dynamics of Hot Jupiters

Thaddeus D. Komacek[1,2]
[1] Department of Physics (Atmospheric, Oceanic and Planetary Physics), University of Oxford, Oxford OX1 3PU, UK; tad.komacek@physics.ox.ac.uk
[2] Department of Astronomy, University of Maryland, College Park, MD 20742, USA
Received 2024 March 25; revised 2025 February 23; accepted 2025 February 25; published 2025 April 1

Abstract

Over the past two decades, a coherent picture has emerged of the atmospheric dynamics of hot Jupiters from a combination of three-dimensional general circulation models and astronomical observations. This paradigm consists of hot Jupiters being spin-synchronized due to their close-in orbit, with a resulting large day-to-night irradiation gradient driving a day-to-night temperature contrast. This day-to-night temperature contrast in turn raises day-to-night pressure gradients that are balanced by a circulation with wind speeds on the order of km s^{-1}. The dominant feature of this circulation is a super-rotating equatorial jet, maintained by eddy-mean flow interactions that pump momentum into the jet. In this work, I explore the dependence of this circulation paradigm on the initial thermal and dynamical conditions in atmospheric circulation models of hot Jupiters. To do so, I conduct MITgcm simulations of the atmospheric circulation of hot Jupiters with both varying initial wind directions and initial temperature profiles. I find that the results are insensitive to the initial conditions, implying that the current paradigm of hot-Jupiter circulation exhibits at most limited hysteresis. I demonstrate that there is a single characteristic wind speed of hot Jupiters for given planetary and atmospheric parameters using an idealized scaling theory, and discuss implications for the interpretation of hot Jupiter observations.

Unified Astronomy Thesaurus concepts: Exoplanet atmospheres (487); Hot Jupiters (753); Planetary atmospheres (1244); Exoplanet atmospheric dynamics (2307)

1. Introduction

Simulations of the atmospheric dynamics of hot Jupiters over the past 22 years since A. Showman & T. Guillot (2002) broadly agree in the key features of their circulation. This standard model of hot-Jupiter atmospheric circulation includes a super-rotating eastward equatorial jet that induces a photospheric eastward hot spot offset and large day-to-night temperature contrasts driven by strong radiative cooling in these hot atmospheres (K. Heng & A. Showman 2015; A. Showman et al. 2020). Though models agree in broad qualitative predictions, intermodel differences exist, especially with regard to the amplitude of variability and potential sensitivity to initial conditions (B. Liu & A. Showman 2013; J. Cho et al. 2015, 2021; J. W. Skinner & J. Y. K. Cho 2022).

The potential for hysteresis (i.e., a dependence of the resulting circulation on initial conditions) is critical to explore in order to determine whether the basic dynamical state of hot Jupiters is robust. Notably, bifurcations in the jet structure depending on the initial conditions have been found in general circulation models (GCMs) of tidally locked temperate terrestrial planets (D. Sergeev et al. 2022), the atmospheric circulation in simulations of sub-Neptunes with deep atmospheres display bistability (H. Wang & R. Wordsworth 2020), and the deep atmosphere has been demonstrated to potentially impact the direction of the equatorial jet on hot Jupiters (J. M. Mendonça 2019; L. Carone et al. 2020) as a result, there is a need to determine if bistability may also occur in the atmospheric dynamics of hot Jupiters.

Determining the extent to which hot-Jupiter dynamics can undergo hysteresis is critical for the interpretation of past, current, and future observations with three-dimensional models. This is especially important for JWST-quality secondary eclipse observations (L.-P. Coulombe et al. 2023) and phase curves (T. Mikal-Evans et al. 2023; T. J. Bell et al. 2024) because our observational sensitivity is now sufficient to constrain the three-dimensional thermal structure of hot Jupiters (M. Mansfield et al. 2020; R. C. Challener & E. Rauscher 2022; M. Hammond et al. 2024). Notably, the baseline expectation from the standard model of hot-Jupiter atmospheric dynamics is for equatorial super-rotation and resulting eastward hot spot offsets near the thermal photosphere (A. Roth et al. 2024), with day-to-night flow dominating at lower pressures, especially for hotter planets (E. Kempton & E. Rauscher 2012; A. Showman et al. 2013; X. Zhang 2020). However, observations do not necessarily find eastward hot spot offsets to be ubiquitous (L. Dang et al. 2018; M. Zhang et al. 2018; T. J. Bell et al. 2021; E. M. May et al. 2022). Proposed explanations for westward hot spot offsets include magnetic effects (T. Rogers 2017), nonsynchronous rotation (E. Rauscher & E. M. R. Kempton 2014), and temperature structures being dominated by a baroclinic wave structure with height maxima that are shifted west of the substellar point near the thermal photosphere (N. Lewis & M. Hammond 2022). One additional potential explanation that has not been explored in detail for hot Jupiters could be a bifurcation in the jet's structure, resulting in weak equatorial flow and strong midlatitude flow, as found for temperate rocky planets (D. Sergeev et al. 2022).

Previous work by K. Shell & I. Held (2004) has shown an abrupt emergence of super-rotation with increasing prescribed momentum forcing strength in axisymmetric idealized models. The K. Shell & I. Held (2004) model may provide an explanation for the bifurcations found in previous tidally

locked planet simulations of D. Sergeev et al. (2022), where the strength of super-rotation depends on the initial conditions, as well as convective and cloud schemes. As in K. Shell & I. Held (2004), there is a need to include a vertical momentum transport term in the model setup in order to reproduce super-rotation in analytic and numerical shallow-water hot-Jupiter models (A. Showman & L. Polvani 2010, 2011). Similarly, three-dimensional studies of the mechanisms governing super-rotation in hot Jupiters require both horizontal and vertical eddy momentum transport by planetary-scale waves to drive super-rotating flow (S. Tsai et al. 2014; M. Hammond & R. Pierrehumbert 2018).

It is plausible that because the day-to-night radiative forcing regime and thus resulting planetary-scale wave pattern of hot Jupiters is different from those of terrestrial planets there could be a significant reduction in the magnitude of any possible dynamical bifurcation. Finally, note that the strong day-to-night forcing of hot Jupiters also leads to numerical limitations in the predictions of equatorial jet speeds due to the potential for over-damping in simulations (D. Koll & T. Komacek 2018; J. W. Skinner & J. Y. K. Cho 2021; M. Hammond & D. Abbot 2022), requiring further exploration of the impacts of both explicit and numerical dissipation on hot-Jupiter atmospheric dynamics.

In this work, I study the potential for hysteresis in the atmospheric dynamics of hot Jupiters near dynamical regime transitions, as has been found previously in simulations of tidally locked temperate terrestrial planets (D. Sergeev et al. 2022). I specifically explore the potential for hysteresis at the dynamical regime transitions where the length scale at which turbulence manifests into jets (i.e., the Rhines scale) and the length scale on which gravity waves are affected by rotation (i.e., the Rossby deformation radius) are comparable to the planetary radius (J. Haqq-Misra et al. 2018). Notably, the atmospheric circulation of hot Jupiters is more strongly forced by irradiation than that of temperate terrestrial planets. This warrants a theoretical comparison between the dynamical states of these objects, as well as suites of numerical experiments in order to determine whether a bifurcation in the strength of super-rotation can manifest similarly at the boundaries of planetary dynamical regimes.

This work is outlined as follows. First, I derive the parameter regimes in which hot Jupiters may undergo transitions between dynamical states where the Rhines scale or Rossby deformation radius is larger or smaller than the planetary radius, and connect these to previously established dynamical regimes for tidally locked planets (Section 2). Then, I detail the numerical setup of and present results from two suites of GCM simulations that study the potential for dynamical regime transitions (Sections 3 and 4). I then interpret these results by developing an idealized scaling theory for the dependence of the equatorial jet speed on momentum forcing (Section 5). I finally discuss the limitations, future work, and outlook (Section 6), and state the key conclusions (Section 7).

2. Potential Dynamical Regime Transitions

2.1. Rhines Scale and Rossby Number

The Rhines scale is $\lambda_\beta \sim \sqrt{U/\beta}$ (P. Rhines 1975), where U is a characteristic wind speed (commonly taken to be the rms, wind speed as in P. Rhines 1975), and $\beta = 2\Omega\cos(\phi)/a$, where Ω is the planetary rotation rate, ϕ is latitude, and a is the planetary radius. Hence, one can express that the Rhines scale is approximately equal to the planetary radius when[3]:

$$\sqrt{\frac{U}{\beta}} = \sqrt{\frac{Ua}{2\Omega\cos(\phi)}} \approx a. \quad (1)$$

One can then calculate the rotation period $P_\beta = 2\pi/\Omega$ at this transition at the equator (i.e., $\phi = 0^\circ$) as a function of planetary radius and wind speed:

$$P_\beta \approx \frac{4\pi a}{U}. \quad (2)$$

I then assume that the hot Jupiter is tidally locked, with a rotation period equal to its orbital period. I use Kepler's third law and the inverse-square law to write the orbital period $P_{\rm orb}$ as a function of stellar luminosity $L_\star$, stellar mass $M_\star$, and incident stellar flux $F_\star$

$$P_{\rm orb} = \frac{\pi^{1/4}}{\sqrt{2GM_\star}}\left(\frac{L_\star}{F_\star}\right)^{3/4}. \quad (3)$$

Equating $P_\beta = P_{\rm orb}$ and substituting the full-redistribution zero-albedo equilibrium temperature $T_{\rm eq} = [F_\star/(4\sigma)]^{1/4}$, I find the dependence of the transition equilibrium temperature where the Rhines scale equals the planetary radius as a function of stellar, planetary, and atmospheric parameters:

$$T_{{\rm eq},\beta} \approx 1300{\rm K}\left(\frac{M_\star}{M_\odot}\right)^{-1/6}\left(\frac{L_\star}{L_\odot}\right)^{1/4} \times \left(\frac{a}{1.38\ \ R_{\rm Jup,eq}}\right)^{-1/3}\left(\frac{U}{4\ \ {\rm km\ \ s^{-1}}}\right)^{1/3}. \quad (4)$$

All stellar values in Equation (4) are normalized to the Solar value, the planetary radius is normalized to that of HD 209458b, and the wind speed is normalized to that in a typical hot Jupiter simulation for HD 209458b-like parameters (T. Komacek et al. 2017).

Note that the above derivation of the equilibrium temperature at which $\lambda_\beta \approx a$ assumed that the characteristic wind speed U was constant, which is not realistic over the broad range of equilibrium temperatures (as well as rotation periods, metallicities, surface gravities, and frictional drag strengths) of hot Jupiters (A. Roth et al. 2024). If I instead use the linear fit for equatorial jet speed with equilibrium temperature from V. Parmentier et al. (2021) of $U_{\rm jet} = (6.2T_{\rm eq}[{\rm K}] - 5075)\ {\rm m\ s^{-1}}$, I find a transition equilibrium temperature of $T_{{\rm eq},\beta} \approx 2166$ K. The uncertainty in equilibrium temperature at which the Rhines scale is approximately equal to the planetary radius motivates the exploration of a broad range of equilibrium temperatures to assess whether dynamical changes can occur across this transition. However, in general if $T_{\rm eq} < T_{{\rm eq},\beta}$, then $\lambda_\beta > a$, and conversely if $T_{\rm eq} > T_{{\rm eq},\beta}$ then $\lambda_\beta < a$. Given that hot Jupiters have $T_{\rm eq} \gtrsim 1000$ K, the range of typical hot Jupiters are

[3] Note that these results depend on the exact definition of the Rhines scale and relevant planetary scale. For instance, one may also define $\lambda_\beta = \pi\sqrt{U/\beta}$, and compare it to the equator-to-pole distance equal to one-quarter of the spherical planetary circumference $\pi a/2$, leading to $\sqrt{\frac{2Ua}{\Omega\cos(\phi)}} \approx a$ rather than Equation (1). In this work, we follow J. Haqq-Misra et al. (2018) and provide relationships comparing approximate dynamical length scales to the planetary radius.

expected to cross this transition between small and large Rhines scales relative to the radius of the planet.

One key caveat to this derivation is that the application of a Rhines scale to characterize the expected width of jets on of hot Jupiters assumes an inverse energy cascade (P. Rhines 1975). However, it is not clear a priori that hot Jupiters (or other tidally locked planets) undergo an inverse cascade in kinetic energy due to their large-scale day-to-night forcing causing the dominant component of the flow to be a wavenumber-1 planetary-scale wave pattern (A. Showman & L. Polvani 2011; M. Hammond & R. Pierrehumbert 2018). As a result, the jet scale may be shaped by the forcing/damping leading to planetary-scale wave propagation and equatorward eddy momentum transport, rather than the β-effect (Y. Wang et al. 2018). This would imply that the Rhines scale cannot be used to characterize the circulation regime of tidally locked planets. Instead, the Rossby deformation radius may be a better indicator of circulation, given its direct relationship to planetary-scale gravity wave speeds.

Note that in the above derivation the regime transition in which the Rhines scale becomes larger/smaller than the planetary radius is approximately equivalent to the regime transition where the Rossby number becomes larger/smaller than one (Y. Wang et al. 2018). If I take $\beta \approx f/a$, the Rhines scale is then $\lambda_\beta \approx \sqrt{\frac{U a}{f}}$. One can then relate the Rhines scale and Rossby number as

$$\frac{\lambda_\beta^2}{a^2} \approx \frac{U}{fa} \equiv \mathrm{Ro}, \tag{5}$$

assuming that the planetary radius is the relevant length scale of the flow. Thus, $\mathrm{Ro} = 1$ when $\lambda_\beta = a$, $\mathrm{Ro} > 1$ when $\lambda_\beta > a$, and $\mathrm{Ro} < 1$ when $\lambda_\beta < a$. As a result, even if the Rhines scale is not applicable to tidally locked exoplanets due to a lack of an inverse cascade (Y. Wang et al. 2018), the derivation here can also be used to determine the dynamical regime via the dominant planetary-scale momentum balance (i.e., advection balancing the day-to-night pressure gradient when $\mathrm{Ro} > 1$, and the Coriolis term balancing the day–night pressure gradient when $\mathrm{Ro} < 1$).

2.2. Rossby Deformation Radius

Next, I explore the dynamical regime transition where the equatorial Rossby deformation radius $\lambda_R \sim a$ (J. Haqq-Misra et al. 2018), where

$$\lambda_R = \sqrt{\frac{NH}{2\beta}}, \tag{6}$$

and here $c_g \sim NH$ is the approximate peak equatorial Kelvin gravity wave speed (A. Showman et al. 2013). As above, I calculate the rotation period P_R at this transition as a function of planetary radius, equilibrium temperature $T_{\rm eq}$, and the specific gas constant R, assuming an isothermal atmosphere at: $T = T_{\rm eq}$[4]

$$P_R \approx \frac{4\pi a \sqrt{c_p}}{R\sqrt{T_{\rm eq}}}. \tag{7}$$

[4] Note that for an isothermal atmosphere, $N = g/\sqrt{Tc_p}$ and $H = RT/g$, implying that $\lambda_R = \sqrt{R\sqrt{T}/(2\sqrt{c_p}\beta)}$.

Here, R and c_p are the specific gas constant and specific heat capacity for a typical H_2 dominated hot-Jupiter atmosphere.

Equating $P_R = P_{\rm orb}$ from Equation (3), I find the dependence of the transition equilibrium temperature between the regimes where the equatorial Rossby deformation radius is greater or larger than the planetary radius as a function of stellar, planetary, and atmospheric parameters:

$$T_{\mathrm{eq},R} \approx 796.1\ \mathrm{K}\left(\frac{M_\star}{M_\odot}\right)^{-1/5}\left(\frac{L_\star}{L_\odot}\right)^{3/10} \times \left(\frac{a}{1.38\quad R_{\mathrm{Jup,eq}}}\right)^{-2/5}. \tag{8}$$

As before, all stellar values in Equation (8) are normalized to Solar and planetary parameters are normalized to HD 209458b-like values. If $T_{\rm eq} < T_{\mathrm{eq},R}$, then $\lambda_R > a$, and conversely if $T_{\rm eq} > T_{\mathrm{eq},R}$ then $\lambda_R < a$.

Given that the equilibrium temperatures of hot Jupiters are $\gtrsim$1000 K, this implies that all typical hot Jupiters[5] should have $\lambda_R < a$. Note that unlike the Rhines scale, the Rossby deformation scale does not depend on the a priori unknown characteristic wind speed, and the theoretical uncertainty is linked instead to the thermal structure and atmospheric composition. Additionally, even though warm Jupiters with $T_{\rm eq} \lesssim 796$ K would have $L_R > a$ if they were tidally locked, they are instead likely rapidly rotating due to the long tidal spin-down timescales at their larger orbital separations (T. Guillot et al. 1996), leading to $L_R \ll a$ and a strongly banded circulation (A. Showman et al. 2015). Note that as shown in A. Showman et al. (2010), the generalized Rossby deformation radius ($\lambda_D = c_g/f \sim NH/f$) is also smaller than the planetary radius for typical hot Jupiters. As a result, hot Jupiters are not expected to undergo a dynamical regime transition where the Rossby deformation radius $\lambda_R \gtrsim a$.

2.3. Dynamical Regimes of Tidally Locked Exoplanets

I now relate the transitions in the dynamical Rhines and equatorial Rossby deformation length scales more broadly to established dynamical regimes which have been published largely in the context of tidally locked temperate terrestrial exoplanets orbiting M dwarf stars (S. Noda et al. 2017; J. Haqq-Misra et al. 2018). First, J. Haqq-Misra et al. (2018) define three dynamical regimes, in order of increasing relative rotation rate:

1. *Slow rotators*. Planets where both the Rhines and equatorial Rossby deformation length scales are larger than the planetary radius (i.e., $\lambda_\beta > a$, $\lambda_R > a$).
2. *Rhines rotators*. Planets where the Rhines scale is smaller than the planetary radius but the Rossby deformation scale is larger than the planetary radius (i.e., $\lambda_\beta < a$, $\lambda_R > a$). Note that in this work I will use the term intermediate rotator to refer to this regime because hot

[5] Note that in this manuscript I am making a distinction between "hot Jupiters" and "ultra-hot Jupiters." Ultra-hot Jupiters may have strong thermal inversions driven by absorption of incoming stellar radiation by metallic species (J. Lothringer et al. 2018), as well as larger specific gas constants due to molecular hydrogen dissociation (T. Bell & N. Cowan 2018), both of which could increase λ_R. However, given that here I neglect the physics of hydrogen dissociation in this work for simplicity, I focus on the hot rather than ultra-hot regime throughout.

Jupiters are not expected to lie in the Rhines rotator regime of J. Haqq-Misra et al. (2018).

3. *Rapid rotators*. Planets where both the Rhines and equatorial Rossby deformation length scales are smaller than the planetary radius (i.e., $\lambda_\beta < a$, $\lambda_R < a$).

As discussed above, I find that depending on their level of irradiation, host star type, planetary radius, and wind speeds, hot Jupiters can have Rhines scales that are less than or larger than the planetary radius. However, the equatorial Rossby deformation radii of hot Jupiters will be smaller than the planetary radius for reasonable ranges of host star type, atmospheric composition, and planetary radius, especially given that more irradiated hot Jupiters typically have larger radii (G. Laughlin et al. 2011; D. Thorngren & J. Fortney 2018). This implies that hot Jupiters can lie in either the rapid rotator regime or an analog of the Rhines rotator regime, which I term the "Rossby" rotator regime, where the Rossby deformation length is smaller than the planetary radius but the Rhines scale is larger than the planetary radius—i.e., $\lambda_\beta > a$, $\lambda_R < a$. In the remainder of this work, I will classify both the Rhines and Rossby rotator regimes as "intermediate" rotators between the slow and rapid rotator limits. The primary reason why intermediate rotator hot Jupiters lie in the Rossby rather than Rhines rotator regime is because their equatorial jet speeds are typically several km s^{-1} rather than the hundreds of m s^{-1} level typical for temperate tidally locked terrestrial planets.

Importantly, hot-Jupiter dynamics do not extend into the slow rotator regime, unlike the dynamical regimes of temperate rocky planets orbiting late-type K dwarf stars or early-type M dwarf stars. The dynamics of hot Jupiters do not extend into the slow rotator regime because they have close-in and short period orbits (and as a result, hot equilibrium temperatures) and because they are found around earlier-type host stars than tidally locked temperate rocky planets. This has been demonstrated from previous large suites of tidally locked hot-Jupiter GCM simulations, which predict super-rotation regardless of the level of irradiation and rotation rate in the limit of weak frictional drag (e.g., X. Tan & T. Komacek 2019; A. Roth et al. 2024).

The four dynamical regimes (named Types I, II, III, and IV) presented in S. Noda et al. (2017) are based off of the dynamical characteristics from simulations of tidally locked terrestrial planets, rather than fundamental dynamical length scales. Type I is characterized by day–night flow and is equivalent to the slow rotator regime of J. Haqq-Misra et al. (2018). Given that hot Jupiters do not lie in the slow rotator regime, they cannot be in the Type I regime of S. Noda et al. (2017) except in cases where drag is sufficiently strong to damp the super-rotating equatorial jet (R. Perna et al. 2010; D. Perez-Becker & A. Showman 2013; H. Beltz et al. 2022), causing the divergent (largely substellar to antistellar flow) component of the circulation to dominate over the rotational (consisting of the equatorial jet and waves) component (M. Hammond & N. Lewis 2021). Instead, as shown in compilations of hot-Jupiter GCMs (K. Heng & A. Showman 2015; A. Showman et al. 2020) the typical circulation in drag-free simulations of hot Jupiters is equivalent to the Type II regime of S. Noda et al. (2017), with a super-rotating equatorial jet and planetary-scale Rossby–Kelvin (Matsuno–Gill) wave pattern (R. Pierrehumbert & M. Hammond 2019).

Simulations of hot Jupiters covering a broad planetary and atmospheric parameter space (e.g., A. Roth et al. 2024) do not typically exhibit circulation similar to Types III and IV of S. Noda et al. (2017), in which the super-rotating equatorial jet becomes unstable (Type III) and transitions to two midlatitude eastward jets (Type IV). As I will discuss later, the lack of Type III-IV circulation on hot Jupiters may be linked to the strong day–night forcing that drives their super-rotating equatorial jet relative to the weaker forcing of temperate terrestrial planets. This is because the presence of super-rotation has a strong dependence on day–night forcing strength (A. Showman & L. Polvani 2011; M. Hammond et al. 2020) and can undergo bifurcations with forcing (K. Shell & I. Held 2004). Notably, the hysteresis found by D. Sergeev et al. (2022) at the boundary of the intermediate rotator and rapid rotator regimes corresponds to the transition between one super-rotating equatorial jet (called "Single Jet" by D. Sergeev et al. 2022, equivalent to Type II of S. Noda et al. 2017) and two midlatitude eastward jets (called "Double Jet" by D. Sergeev et al. 2022, equivalent to Type IV of S. Noda et al. 2017).

3. Numerical Methods

3.1. Numerical Setup

In this work, I focus on hot Jupiters where $T_{\rm eq} \approx T_{{\rm eq},\beta}$ in order to study how the chosen initial conditions affect the resulting circulation regime at the transition between intermediate rotators (i.e., Rossby or Rhines rotators) and rapid rotators. I conduct GCM simulations with the cubed-sphere MITgcm (A. Adcroft et al. 2004), using similar approaches to those outlined in detail in T. Komacek & A. Showman (2016) and T. Komacek et al. (2017). I do not include additional effects such as magnetic drag (R. Perna et al. 2010; T. Rogers & A. Showman 2014; H. Beltz et al. 2022) or hydrogen dissociation and recombination (X. Tan & T. Komacek 2019; A. Roth et al. 2021), but in some cases I do include a simplified uniform basal drag term (B. Liu & A. Showman 2013), the strength of which is freely varied. Specifically, I conduct two suites of GCM simulations, described further below:

1. Varying initial wind strength and direction for two basal drag strengths. This suite of GCMs builds directly upon B. Liu & A. Showman (2013), extending their results to smaller basal drag timescales and longer model runtimes.
2. Varying initial temperature profile for a range of equilibrium temperatures, crossing from the intermediate rotator to rapid rotator regimes.

3.1.1. Varying Initial Wind Profile

In Suite 1, I study the effect of varying initial wind velocity using an idealized GCM setup adapted from T. Komacek & A. Showman (2016) with Newtonian cooling setting the heating/cooling rates in the dynamical core. I fix the planetary parameters to only study one planetary case, with an HD 209458b-like radiative equilibrium temperature profile (N. Iro et al. 2005). In these Newtonian cooling models, the top boundary radiative equilibrium day–night temperature contrast and top boundary radiative timescales are free parameters, which I fix to $\Delta T_{\rm eq,top} = 1000$ K and $\tau_{\rm rad,top} = 10^4$ s, respectively. The radiative equilibrium day–night temperature contrast then decreases logarithmically with increasing pressure until a maximum pressure of 10 bars, at pressures above which the radiative equilibrium day–night temperature contrast is fixed to zero. Similarly, the radiative timescale increases with

Table 1
Planetary and Atmospheric Properties Assumed for Both Suites of GCM Simulations Presented in this Work, Along with Atmospheric and Numerical Parameter Choices Common to all Simulations

Parameter	Value
Suite 1 parameters	
Initial peak zonal wind velocity	[0, +1, −1] m s^{-1}
Basal drag constant (k_F)	[10^{-2}, 10^{-3}] day^{-1}
Rotation period	3.5 days
Radius	9.43 × 10^7m
Gravity	9.36 m s^{-2}
Top radiative equilibrium day–night temperature contrast	1000 K
Maximum pressure of top day–night temperature contrast	10^{-3} bars
Bottom radiative equilibrium day–night temperature contrast	0 K
Minimum pressure of bottom day–night temperature contrast	10 bars
Top radiative timescale	10^4 s
Maximum pressure of top radiative timescale	10^{-2} bars
Bottom radiative timescale	10^7 s
Minimum pressure of bottom radiative timescale	10 bars
Basal drag minimum pressure	10 bars
Horizontal resolution	C16
Newtonian cooling time step	45 s
Suite 2 parameters	
Suite 2(a)	
Equilibrium temperature	[1100, 1200, 1300, 1400, 1500] K
Rotation period	[5.93, 4.57, 3.59, 2.88, 2.34] days
Dynamical time step	15 s
Radiative time step	150 s
Suite 2(b)	
Equilibrium temperature	[1600, 1700, 1800, 1900, 2000, 2100, 2200, 2300, 2400, 2500] K
Rotation period	[1.93, 1.61, 1.35, 1.15, 0.99, 0.85, 0.74, 0.65, 0.57, 0.51] days
Dynamical time step	5–15 s
Radiative time step	20–30 s
All of Suite 2	
Initial temperature	[$T_{eq}/\sqrt{2}$, $\sqrt{2}T_{eq}$]
Radius	9.87 × 10^7 m
Gravity	9.30 m s^{-2}
Drag constant (k_F)	0
Internal temperature	100 K
Horizontal resolution	C32
Parameters common to all simulations	
Specific heat capacity	1.3 × 10^4 J kg^{-1} K^{-1}
Specific gas constant	3714 J kg^{-1} K^{-1}
Vertical layers	40
Upper boundary pressure	0.183 mbars
Lower boundary pressure	200 bars
Shapiro filter order	4
Shapiro filter timescale	25 s

increasing pressure as a power law until a maximum pressure of 10 bars, at pressures above which it is fixed to 10^7 s. All other Newtonian cooling values and planetary parameters are kept the same as in T. Komacek & A. Showman (2016) (see Table 1).

Similarly to the shallow-water and three-dimensional GCM models with Newtonian cooling of B. Liu & A. Showman (2013), I conduct simulations for three separate assumptions of initial wind speeds, either no winds ("rest"), an everywhere eastward barotropic flow, or a westward barotopic flow. In both of the latter cases, the flow is initialized with a maximum velocity at the equator of $+1\,\mathrm{km\,s^{-1}}$ ("eastward") and $-1\,\mathrm{km\,s^{-1}}$ ("westward"), and the winds decay with latitude. Figure 1 shows the initial wind profiles for these two cases with eastward and westward initial flow. In both cases, the wind profiles vary only as a function of latitude and are fixed in both longitude and pressure.

In this set of simulations with varying initial wind profiles, I also include a basal drag which is horizontally uniform but increases in strength from a given pressure toward the bottom of the domain. I consider two levels of basal drag, with a maximum strength a factor of 10 and a hundred times weaker than the nominal value in B. Liu & A. Showman (2013), as described further below. I do so in order to determine the level of impact of drag on the atmospheric circulation, extending the results of B. Liu & A. Showman (2013) to include a full suite of simulations with weaker frictional drag, as well as varying the initial wind profile. Note that B. Liu & A. Showman (2013) state that they explore cases with varying frictional drag strength, but they do not present a systematic exploration of the impact of frictional drag strength on the resulting dynamics.

The "basal" drag is parameterized as in B. Liu & A. Showman (2013). This drag is only applied in the deep atmosphere at pressures above 10 bar, motivated by the frictional interaction between the atmosphere and the relatively quiescent interior. The drag force is parameterized as a Rayleigh drag

$$\mathcal{F}_d = -k_F \boldsymbol{v} = -\frac{\boldsymbol{v}}{\tau_{\mathrm{drag}}}, \tag{9}$$

where k_F increases linearly with pressure from zero at 10 bars to a maximum value at the bottom of the domain at a pressure of 200 bars (T. Komacek & A. Showman 2016). I conduct simulations with two values of the maximum k_F (i.e., the drag constant at 200 bars) of 10^{-2} and $10^{-3}\,\mathrm{day^{-1}}$. These values of k_F correspond to equivalent minimum basal drag timescales of $\tau_{\mathrm{drag}} = 8.64 \times 10^6$ and 8.64×10^7 s. These are weaker basal drag coefficients (longer drag timescales) than used in B. Liu & A. Showman (2013), who take $k_F = 10^{-1}\,\mathrm{day^{-1}}$ for their primary suite of three-dimensional models. This results in a total of six simulations in Suite 1, three cases with varying initial winds for each of the two chosen drag strengths.

3.1.2. Varying Initial Temperature

In Suite 2, I conduct a suite of simulations crossing the intermediate rotator to rapid rotator transition with varying irradiation, here written as the full-redistribution equilibrium temperature T_{eq}. For each case at a given T_{eq}, I conduct two simulations with varying initial temperature, one "hot start" and one "cold start,"[6] in order to determine whether hot Jupiters could exhibit a dependence on initial conditions at the intermediate-rapid rotator regime transition as was found for TRAPPIST-1e in D. Sergeev et al. (2022). In all simulations for

[6] Since these are not evolutionary calculations, the nomenclature is similar but not equivalent to the hot start and cold start in gas giant formation models (e.g., D. Berardo et al. 2017; A. Youdin & Z. Zhu 2025).

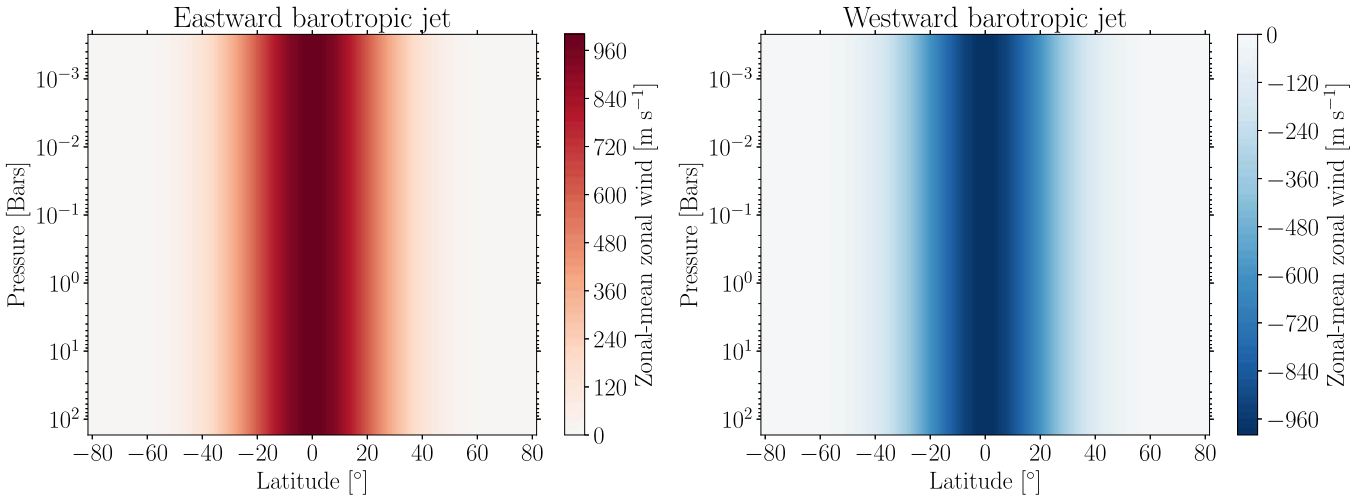

Figure 1. Initial zonal-mean wind profiles for GCM cases in Suite 1 with varying initial wind direction. The two maps share a color scale, with red representing eastward zonal-mean zonal wind speeds, blue representing westward wind speeds, and white zero zonal-mean zonal wind. In both cases, the initial jet is prescribed to be barotropic, with no variation in pressure.

Suite 2, I couple the MITgcm to the double-gray version of the DISORT (K. Stamnes et al. 1988; A. Kylling & K. Stamnes 1992) two-stream radiative transfer scheme, as used in T. Komacek et al. (2017). The model setup is similar to that in T. Komacek et al. (2017), including the choices of double-gray visible and infrared band opacities. This setup is relevant for an HD 209458b-like H_2/He dominated atmosphere, except for the choices of equilibrium temperature and initial temperature profile, as discussed further below (also see Table 1). I do not include frictional drag at any point in the atmosphere for those cases in Suite 2 with a varying initial temperature profile because drag (especially deep basal drag) has previously been shown to potentially limit hysteresis in hot-Jupiter GCM simulations (B. Liu & A. Showman 2013, see also Suite 1).

I conduct two subgrids of simulations in Suite 2. In Suite 2(a), I conduct simulations varying instellation to cross $T_{\mathrm{eq},\beta}$ in steps of 100 K (1100, 1200, 1300, 1400, 1500 K crossing the expected $T_{\mathrm{eq},\beta} \approx 1300$ K assuming that wind speed does not scale steeply with instellation in this regime). I keep the simulation parameter space focused on relatively cool temperatures in order to avoid the impacts of hydrogen dissociation and recombination (T. Bell & N. Cowan 2018; X. Tan & T. Komacek 2019; A. Roth et al. 2021) and Lorentz forces due to the internal magnetic field coupling to the flow (R. Perna et al. 2010; K. Batygin et al. 2013; E. Rauscher & K. Menou 2013; T. Rogers & A. Showman 2014; H. Beltz et al. 2022) at higher temperatures, which are not included in these idealized simulations. In these simulations, I keep the orbital period equal to the rotation period and include the variation in rotation period consistently with Kepler's third law assuming a Sun-like star—as a result, the varying T_{eq} corresponds to varying $P_{\mathrm{orb}} = P_{\mathrm{rot}}$ (5.93, 4.57, 3.59, 2.88, 2.34 days, decreasing with increasing T_{eq}). For each set of (T_{eq}, P_{rot}) I vary the isothermal initial temperature profile, where cold start cases have $T = T_{\mathrm{eq}}/\sqrt{2}$ and hot start cases have $T = T_{\mathrm{irr}} = \sqrt{2}\,T_{\mathrm{eq}}$. This results in a total of 10 simulations, with two initial temperature profiles for each of the five assumed combinations of (T_{eq}, P_{rot}).

In Suite 2(b), I extend the grid of simulations in Suite 2(a) to cover the potential for a higher transition equilibrium temperature if the linear fit for the equatorial jet speed from V. Parmentier et al. (2021) is used rather than a fixed jet speed as in Equation (4). This extension covers equilibrium temperatures from 1600 to 2500 K, again in 100 K increments, with both hot and cold start cases using the same prescription as in Suite 2(a), resulting in 20 additional simulations for a total of 30 in Suite 2. These simulations in Suite 2(b) also include a varying planetary rotation period with equilibrium temperature assuming a Sun-like star as in Suite 2(a). Table 1 details the planetary and numerical parameter choices for both Suites 2(a) and 2(b).

3.2. Numerical Details

All of the simulations presented in the manuscript are conducted to sufficient run time to enable convergence in wind profiles, as measured via the domain-integrated and level-by-level kinetic energy. Simulations in Suite 1 with varying initial wind speed are run to ∼25,000 Earth days, with these long run timescales enabled by the idealized Newtonian cooling scheme. Note that these model runtimes are significantly longer than those presented in B. Liu & A. Showman (2013), which were only conducted to ∼1000 Earth days. The simulations in Suite 2(a) with varying initial temperature profiles are each conducted for ∼5000 days to reach convergence, while the simulations in Suite 2(b) are each conducted to a shorter end model time of ∼1500 days.

The simulations with varying initial wind speed have a low cubed-sphere resolution of C16 (approximately 64 x 32 x 40 in Cartesian coordinates). Simulations with varying initial temperature have a higher resolution of C32 (approximately 128 x 64 x 40). All simulations in both model Suites 1 and 2(a) have a dynamical time step of 15 s, while some simulations in Suite 2(b) have shorter dynamical time steps, as low as 5 s, as well as shorter radiative time steps, as low as 20 s, for numerical stability. All numerical results shown in the following sections for cases in both Suite 1 and Suite 2(a) are averaged over the last 500 days of model time, while those in Suite 2(b) are averaged over the last 350 days of model time.

4. Numerical Results

4.1. Varying Initial Wind Profile

I first describe results from the suite of simulations with varying initial wind profiles for two separate basal drag

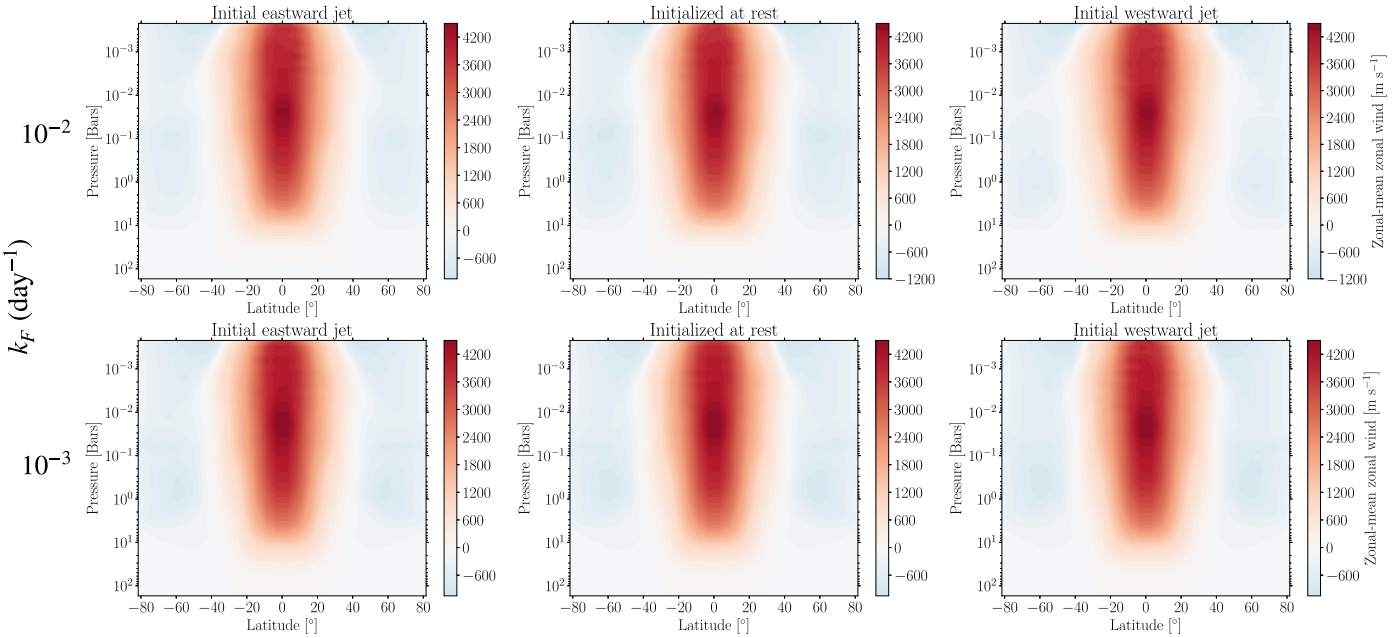

Figure 2. Zonal-mean zonal wind profiles from simulations with different initial wind patterns. The left-hand column shows simulations initialized with a barotropic eastward jet, the middle column shows simulations initialized at rest, and the right-hand column shows simulations initialized with a barotropic westward jet. The top row corresponds to simulations with a maximum basal drag parameter of $k_F = 10^{-2}$ day^{-1}, and the bottom row corresponds to simulations with a weaker basal drag parameter of $k_F = 10^{-3}$ day^{-1}. All plots share colormap limits. I find that the zonal-mean zonal wind from simulations for a given drag parameter with different initial wind profiles are nearly identical.

strengths, the model setup of which is outlined in detail in Section 3.1.1. Figure 2 shows zonal-mean zonal wind profiles from each of the six simulations with varying initial wind profile (columns) and maximum basal frictional drag coefficient (rows). All simulations display the characteristic hot-Jupiter zonal-mean circulation pattern characterized by a super-rotating equatorial jet (A. Showman & L. Polvani 2011), regardless of whether the initial wind profile is super-rotating or subrotating.

The strength of the simulated jet depends slightly on the maximum drag coefficient k_F, as simulations with stronger drag (higher k_F) have weaker peak wind speeds. For instance, the case begun from rest with $k_F = 10^{-2}$ day^{-1} has a peak zonal-mean zonal wind speed of 4366.9 m s^{-1}, while the case started from rest with $k_F = 10^{-3}$ day^{-1} has a faster peak zonal-mean zonal wind speed of 4495.1 m s^{-1} (a 2.85% increase). However, all simulations at a given drag strength show zonal-mean zonal wind profiles which are nearly identical regardless of initial wind profiles. The largest difference in maximum zonal-mean zonal wind speed between simulations at a given drag strength is 32.4 m s^{-1} (a 0.742% variation), which occurs in the cases with $k_F = 10^{-2}$ day^{-1}. Meanwhile, the cases with $k_F = 10^{-3}$ day^{-1} show at most a 0.216% variation in zonal-mean zonal winds.

For completeness, I also show the near-photospheric (81.5 mbar) temperature and wind maps from the same six simulations with varying initial wind profile and frictional drag strength in Figure 3. As for the zonal-mean zonal wind speeds, the wind and temperature patterns on an isobar display very small intermodel differences. All cases have an eastward hot spot offset driven by the super-rotating equatorial jet Doppler-shifting the planetary-scale wave pattern (M. Hammond & R. Pierrehumbert 2018). All cases also have their coldest regions at Rossby gyres in the midlatitudes, and a nearly identical flow pattern everywhere for a given k_F. Overall, these small intermodel differences in jet speeds and temperature structures with varying initial wind profiles agree well with the findings of B. Liu & A. Showman (2013), extending their results to weaker drag and longer runtimes. This implies that the strength of basal drag does not significantly impact the near-photospheric jet structure of hot Jupiters. Overall, I find no evidence from this limited set of GCM simulations that the atmospheric circulation in three-dimensional simulations of hot-Jupiter dynamics displays a dependence on the initial wind profile.

4.2. Varying Initial Temperature Profile

4.2.1. Time-averaged Temperature and Winds

I next turn to describe results from the second suite of simulations with varying initial temperature profile, the model setup of which is outlined in Section 3.1.2. Figure 4 shows temperature and wind maps near the photosphere from all 10 GCM simulations in Suite 2(a) with varying equilibrium temperature (rows) from 1100 to 1500 K for cold and hot initial temperature profiles (columns), and Figure 5 shows the equivalent temperature and wind maps from the 20 GCM simulations in Suite 2(b).

Increasing equilibrium temperature increases the dayside temperature and day-to-night temperature contrast leading to a corresponding increase in the speed of atmospheric winds, as expected (D. Perez-Becker & A. Showman 2013). Simulations for both cold and hot start cases at a given equilibrium temperature (i.e., in a given row) display similar horizontal temperature structures and wind patterns. This implies that there is no key change in the near-photospheric thermal structure across the theoretical regime transition where the Rhines scale is greater than or less than the planetary radius previously derived in Equation (4) (Suite 2(a)), or when

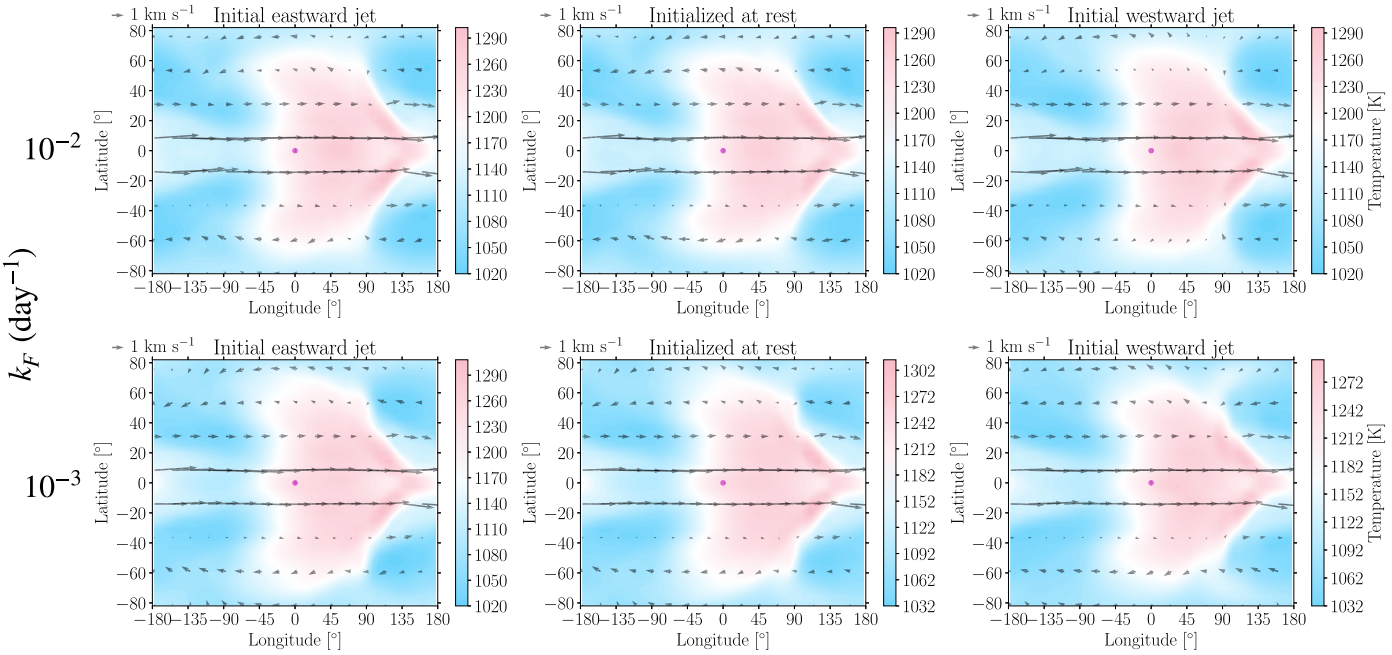

Figure 3. Temperature (colors) and wind (quivers) maps at 81.5 mbar pressure from simulations with different initial wind patterns. The left-hand column shows simulations initialized with a barotropic eastward jet, the middle column shows simulations initialized at rest, and the right-hand column shows simulations initialized with a barotropic westward jet. The top row corresponds to simulations with maximum basal drag parameter of $k_F = 10^{-2}$ day^{-1}, and the bottom row corresponds to simulations with a weaker maximum drag parameter of $k_F = 10^{-3}$ day^{-1}. All plots share colormap limits, but the colorbar limits are kept separate for each plot in order to display small intermodel differences. I find that the temperature pattern from simulations with different initial wind profiles are nearly identical for a given drag parameter, as expected given their similar jet structure.

including a linear dependence of wind speed on equilibrium temperature (Suite 2(b)).

The corresponding zonal-mean zonal winds as a function of latitude and pressure from simulations with varying equilibrium temperature for cold and hot initial thermal profiles are shown for Suite 2(a) in Figure 6 and for Suite 2(b) in Figure 7. The zonal-mean zonal wind increases with increasing equilibrium temperature due to the increasing day-to-night forcing amplitude, as expected. Additionally, there is no significant change in the zonal-mean zonal wind structure between cold and hot start cases, as was found for the near-photospheric horizontal thermal structure. This implies that there is no bifurcation between single jet and double jet regimes on hot Jupiters crossing the theoretical $L_\beta \sim a$ threshold. Overall, I find no significant evidence for a dependence of the jet structure on initial conditions for hot Jupiters that was found in the terrestrial planet simulations of D. Sergeev et al. (2022). However, note that this may not apply to *ultra-hot* Jupiters because the high-latitude flow (but not the equatorial jet) may be sensitive to initial conditions and including molecular hydrogen dissociation and recombination, which is neglected here, may affect the potential for hysteresis (see Section 6.1).

4.2.2. Spatiotemporal Averages

The above description of results from Suites 2(a) and 2(b) demonstrates that there is no dependence of the temperature or wind pattern on the initial thermal structure from simulations covering equilibrium temperatures from 1100 to 2500 K. However, these simulations have not been demonstrated to cross a predicted regime transition from intermediate to rapid rotators with varying equilibrium temperature. To demonstrate that these simulations cross a theoretical regime transition, in Figure 8 I show the numerically calculated Rossby number using the GCM simulations from Suite 2. Note that $\mathrm{Ro} \approx (\lambda_\beta/a)^2$ from Equation (5). As a result, the shaded region corresponds to the "intermediate" rotator regime with $\mathrm{Ro} > 1$ and equivalently $\lambda_\beta/a > 1$, while values of $\mathrm{Ro} < 1$ and equivalently $\lambda_\beta/a < 1$ correspond to the rapid rotator regime. I find that, as expected from the scaling in Equation (4), the transition between the intermediate and rapid rotator regimes occurs at $T_{\rm eq} \approx 1300$ K if the equatorial jet speed is taken to be the characteristic wind speed. Conversely, the slower global rms wind speeds imply that if the global rms winds are taken as the characteristic wind speeds, then all cases lie in the rapid rotator regime with $\mathrm{Ro} < 1$ and $\lambda_\beta/a < 1$. However, note that the fact that the simulations cross the $\mathrm{Ro} = 1$ and equivalently $\lambda_\beta/a \approx 1$ threshold does not necessarily imply that they cross an actual dynamical regime transition, as in J. Haqq-Misra et al. (2018), Y. Wang et al. (2018), and D. Sergeev et al. (2022), because all simulations have broadly the same dynamical characteristics, including a single super-rotating equatorial jet.

In order to more quantitatively demonstrate this finding that the atmospheric dynamics of hot Jupiters exhibit limited dependence on initial thermal conditions, I show the dayside and nightside temperature and zonal-mean zonal winds from the cases with a hot initial thermal profile ("hot start," solid lines) and cold initial thermal profile ("cold start," dashed lines) for the subset of cases from in Suite 2(a) in Figure 9. If the simulations displayed a strong dependence on initial conditions, Figure 9 would show significant differences between the cold start and hot start cases. Instead, I find that the near-photospheric temperature and zonal-mean zonal wind have a nearly equivalent dependence on equilibrium temperature, regardless of the initial temperature profile. The small remaining differences between the cases are due to ongoing

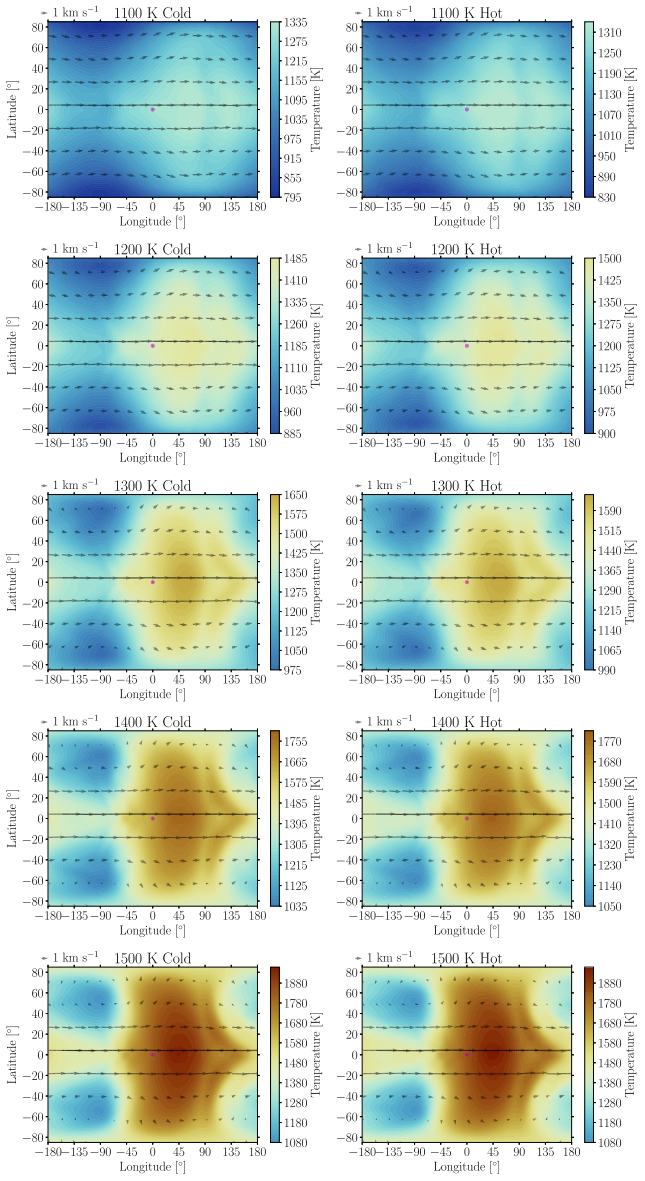

Figure 4. Temperature (colors) and wind (quivers) maps at 81.5 mbar pressure from Suite 2(a) with varying equilibrium temperature (rows) and initial conditions (columns). Each map shares a color scale with Figure 5, and the colorbar beside the map displays the range of temperatures contained within the map. A 1 km s^{-1} quiver is displayed in the upper left-hand corner of each map. I find that the near-photospheric temperature and winds are nearly identical in both the cases with cold and hot initial conditions. This implies that there is no hysteresis in the photospheric climate state across the intermediate rotator-rapid rotator transition using the dynamical regime definitions of J. Haqq-Misra et al. (2018).

radiative adjustment toward equilibrium, causing the cold start cases to have slightly smaller day–night temperature differences and wind speeds than the hot start cases even after 5000 days of model time. However, there are no distinct branches for the cold and hot start cases in either temperature or winds. Additionally, as shown in Figures 4 and 6, there is no change in the temperature pattern or wind structure between the cold and hot start cases in Suite 2(a). These numerical results imply that the Rhines scale does not control the dynamical regime of hot Jupiters. This can be interpreted as a demonstration that the circulation of hot Jupiters is controlled by the large-scale day-to-night forcing, rather than an inverse turbulent energy cascade (N. T. Lewis 2025, personal communication).

5. Analytic Theory Relating Forcing to Characteristic Wind Speeds

Here, I use an analytic approach broadly inspired by K. Shell & I. Held (2004) to investigate the steady-state relationship between momentum forcing and the horizontal winds on hot Jupiters. To do so, I use a two-dimensional one-and-a-half layer shallow-water model with day-to-night forcing prescribed as a Newtonian heating/cooling term from D. Perez-Becker & A. Showman (2013). Here, the applied forcing (torque) is balanced by frictional drag, here assumed to be Rayleigh drag as in the numerical simulations in Suite 1 presented above, along with momentum exchange with the lower layer. Thus, the momentum forcing F is equal to

$$F = \frac{(h_{\rm eq} - h)}{\tau_{\rm rad}} \frac{u}{h} + \frac{u}{\tau_{\rm drag}}, \tag{10}$$

where h is the layer thickness, $h_{\rm eq}$ is the radiative equilibrium layer thickness, $\tau_{\rm rad}$ is the radiative timescale, u is the zonal wind, and $\tau_{\rm drag} = k_F^{-1}$ is the drag timescale. Note that the day-to-night forcing term (first term on the right-hand side of Equation (10)) and the frictional drag term (second term on the right-hand side of Equation (10)) must balance in a global average sense for the circulation to be steady state with $F = 0$. This is analogous to considering the global circulation as a heat engine (G. Schubert & J. Mitchell 2013; D. Koll & T. Komacek 2018). As a result, one can consider F as the "residual" forcing that can either increase or decrease wind speeds toward an equilibrium value.

I now use an approach similar to D. Perez-Becker & A. Showman (2013) to scale this expression to relate F to the characteristic horizontal wind speed $u \sim U$ and the characteristic layer thickness $h \sim H$

$$F \sim \frac{(\Delta h_{\rm eq} - \Delta h)}{\tau_{\rm rad}} \frac{U}{H} + \frac{U}{\tau_{\rm drag}} \approx \frac{(h_{\rm eq} - \Delta h)}{\tau_{\rm rad}} \frac{U}{H} + \frac{U}{\tau_{\rm drag}}, \tag{11}$$

where Δh is the characteristic day-to-night layer height contrast, $\Delta h_{\rm eq}$ is the characteristic day-to-night height contrast in radiative equilibrium, and I have assumed a large day-to-night radiative equilibrium height contrast $\Delta h_{\rm eq} \sim h_{\rm eq}$.

Next, I use the scaled steady-state momentum balance from D. Perez-Becker & A. Showman (2013) to relate the day–night height contrast to planetary and model parameters:

$$g \frac{\Delta h}{a} \sim \frac{U}{\tau_{\rm drag}} + fU. \tag{12}$$

The left-hand side of Equation (12) is the pressure gradient driven by the day-to-night height contrast (where a is the planetary radius), the first term on the right-hand side is frictional drag, and the second term on the right-hand side is the Coriolis force (where $f = 2\Omega \sin\phi$ is the Coriolis parameter). Solving for Δh, substituting it into Equation (11), and collecting terms, I find a relationship between the momentum

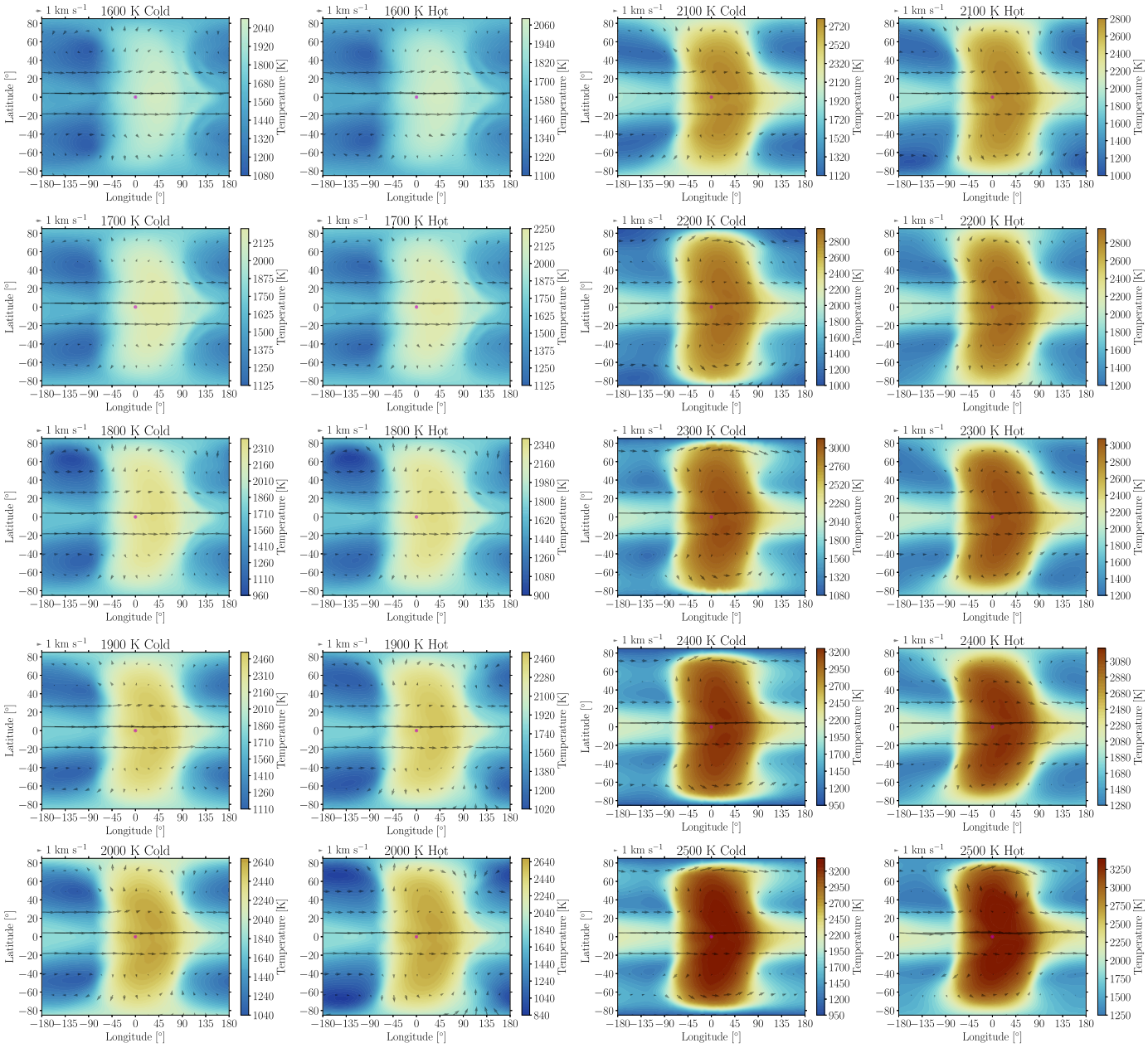

Figure 5. As in Figure 4, but here showing temperature (colors) and wind (quivers) maps at 81.5 mbar pressure from the simulations in Suite 2(b) with varying equilibrium temperature (rows) and initial conditions (columns). Each map shares a color scale with Figure 4, and the colorbar beside the map displays the range of temperatures contained within the map. A 1 km s^{-1} quiver is displayed to the upper left-hand corner of each map.

forcing F and the characteristic horizontal winds U

$$F \sim \frac{U}{H\tau_{\rm rad}}\left(h_{\rm eq} - \frac{afU}{g}\right) + \frac{U}{\tau_{\rm drag}}\left(1 - \frac{aU}{gH\tau_{\rm rad}}\right) \sim \frac{U}{\tau_{\rm rad}}\left(\frac{h_{\rm eq}}{H} - \frac{fU\tau_{\rm wave}^2}{a}\right) + \frac{U}{\tau_{\rm drag}}\left(1 - \frac{U\tau_{\rm wave}^2}{a\tau_{\rm rad}}\right), \quad (13)$$

where in the latter expression I have substituted $\tau_{\rm wave} \sim a/\sqrt{gH}$ (D. Perez-Becker & A. Showman 2013). Note that in the limit where $\tau_{\rm rad} \to \infty$, Equation (13) reduces to $F \sim U/\tau_{\rm drag}$, which is the Rayleigh drag term. Similarly, in the limit where $\tau_{\rm drag} \to \infty$, Equation (13) reduces to $F \sim \frac{h_{\rm eq}U}{H\tau_{\rm rad}} - \frac{fU^2\tau_{\rm wave}^2}{a\tau_{\rm rad}}$ (i.e., only the first term on the right-hand side is retained).

Figure 10 shows the relationship between momentum forcing and characteristic horizontal wind speeds from Equation (13) for varying $\tau_{\rm rad}$ and $\tau_{\rm drag}$ using planetary parameters $(a, f, g, T_{\rm eq})$ relevant for the equator of HD 209458b and assuming that $h_{\rm eq} \sim H \sim RT_{\rm eq}/g$. The local minimum in forcing corresponds to an equilibrium characteristic horizontal wind speed

$$U_e \sim \frac{a}{\tau_{\rm wave}^2}\left(\frac{\frac{h_{\rm eq}}{H} + \frac{\tau_{\rm rad}}{\tau_{\rm drag}}}{f + \frac{1}{\tau_{\rm drag}}}\right), \quad (14)$$

which is shown by the dotted lines in Figure 10. Positive forcing (increasing the angular momentum) corresponds to characteristic horizontal wind speeds that are slower than the

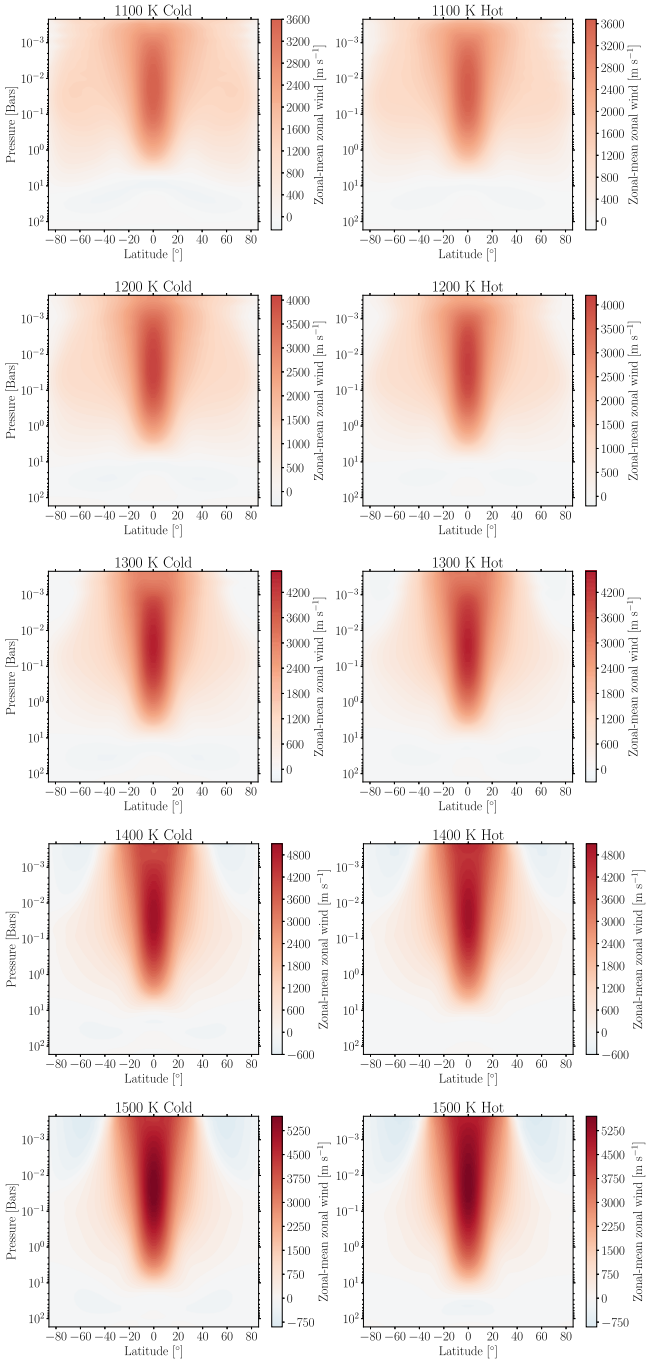

Figure 6. Zonal-mean zonal wind from Suite 2(a) with varying equilibrium temperature (rows) and initial conditions (columns). Each map shares a color scale with Figure 7, and the colorbar displays the range of zonal-mean zonal wind speeds in each plot. White corresponds to zero zonal-mean zonal wind. I find that all cases have a super-rotating eastward equatorial jet, with the zonal-mean zonal wind pattern nearly identical between the cases with cold and hot initial conditions.

equilibrium value. Conversely, negative forcing corresponds to characteristic horizontal wind speeds that are faster than the equilibrium value in Equation (14). Note that U_e is independent of the radiative timescale $\tau_{\rm rad}$ in the case with $\tau_{\rm drag} = \infty$. This is because in the limit of weak drag ($\tau_{\rm drag} \to \infty$), Equation (14) implies that $U_e \to \frac{h_{\rm eq} a}{H f \tau_{\rm wave}^2}$ independent of $\tau_{\rm rad}$. In general, an equilibrium wind speed can only be reached at the minimum in forcing because at more positive values of F (i.e., $U < U_e$) the forcing would drive wind speeds faster, toward equilibrium. Conversely, at more negative values of F (i.e., $U > U_e$) the forcing would slow wind speeds, again toward their equilibrium value.

The theory presented here is a linear scaling theory, and thus does not incorporate nonlinear feedbacks (e.g., hydrogen dissociation and recombination or other processes acting like moisture) that could amplify dependencies on initial conditions. This simplified theory notably does not explain why sub-Neptune GCMs (H. Wang & R. Wordsworth 2020) and rocky planet GCMs (D. Sergeev et al. 2022) show bistability, while the hot-Jupiter GCMs presented in this work and others (e.g., A. Showman et al. 2020) do not. Further work is needed to incorporate the impacts of latent heat and latitude-dependent forcing to determine whether simple analytic theory along the lines of K. Shell & I. Held (2004) can explain the transition between single jet and double jet regimes on tidally locked terrestrial planets. In addition, further work is needed to include the effects of hydrogen dissociation and recombination (T. Komacek & X. Tan 2018; A. Roth et al. 2021) to explore whether the circulation of ultra-hot Jupiters (as opposed to cooler hot Jupiters) could exhibit hysteresis.

6. Discussion

6.1. Limitations and Future Work

This work directly builds upon the previous detailed study by B. Liu & A. Showman (2013) of the impact of initial conditions on the atmospheric dynamics of hot Jupiters though the following: first, incorporating a broader range of weak basal drag strengths in a suite of Newtonian cooling models; second, conducting a suite of simulations coupled to more realistic double-gray radiative transfer; and third, directly searching for a dependence of initial conditions on the atmospheric circulation at potential dynamical regime transitions. However, this work is limited in both model complexity and the range of initial conditions considered. Here, I chose to use either Newtonian heating/cooling or double-gray radiative transfer in order to conduct a broad range of models, but these simulations are not as complex as those with more realistic nongray radiative transfer. E. Lee et al. (2021) demonstrated that nongray radiative transfer (either using the picket fence or correlated-k approximations) provides a significant increase in model realism over double-gray approaches. Future work studying the potential for hysteresis in atmospheric circulation models should couple to nongray radiative transfer, as is common in current state-of-the-art hot-Jupiter GCMs (I. Dobbs-Dixon & E. Agol 2013; T. Kataria et al. 2015; B. Drummond et al. 2018a; D. Christie et al. 2021; V. Parmentier et al. 2021; A. Schneider et al. 2022; I. Malsky et al. 2024; X. Tan et al. 2024). In addition, the varied initial conditions in this work only covered the initial equatorial jet speed and temperature profile, and I did not consider different shear profiles for the initial velocity pattern. Furthermore, it would be more appropriate to search for hysteresis using simulations with an initial hot and cold condition that are then progressively adjusted to lower and higher values of instellation, respectively (e.g., J. H. Checlair et al. 2019; M. Turbet et al. 2021), because the simulations in this work simply test the potential for bifurcations rather than diagnosing a possible hysteresis loop.

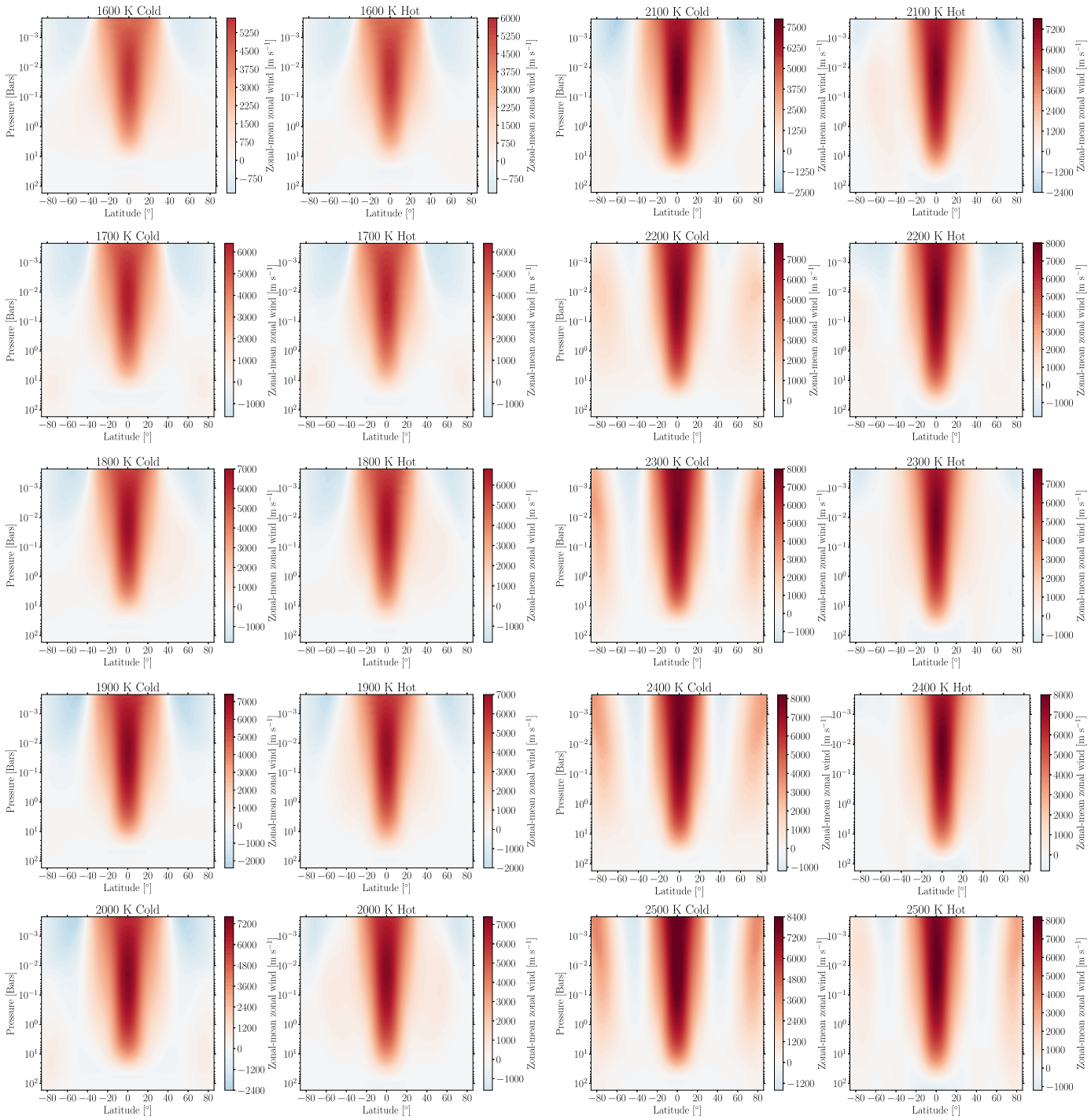

Figure 7. As in Figure 6, but here showing zonal-mean zonal wind from Suite 2(b) with varying equilibrium temperature (rows) and initial conditions (columns). Each map shares a color scale with Figure 6, and the colorbar displays the range of zonal-mean zonal wind speeds in each plot. White corresponds to zero zonal-mean zonal wind.

The horizontal and vertical resolution in the simulations presented here is limited, with only 40 vertical layers and cubed-sphere horizontal resolutions of C16 and C32 for the two model suites presented. In this work, the resolution was kept low in order for these simulations to be integrated over a long model time (25,000 and 5000 days in Suites 1 and 2, respectively) and reach steady state. However, future work at a higher horizontal spatial resolution is required to more directly compare with predictions of circulation from high-resolution hot-Jupiter GCMs with Newtonian cooling (J. Cho et al. 2021; J. W. Skinner & J. Y. K. Cho 2022), which display a much less steady circulation than previous low-resolution work coupled to double-gray radiative transfer (T. Komacek & A. Showman 2016). Longitudinal dissipation via numerical filters and hyperviscosity at low resolution has also been found to affect the resulting dynamics (e.g., K. Heng et al. 2011; D. Koll & T. Komacek 2018; D. Christie et al. 2024), and any resulting hysteresis may be affected by the combination of horizontal resolution and applied numerical dissipation. In addition, simulations with a higher vertical resolution are required in order to determine if hot

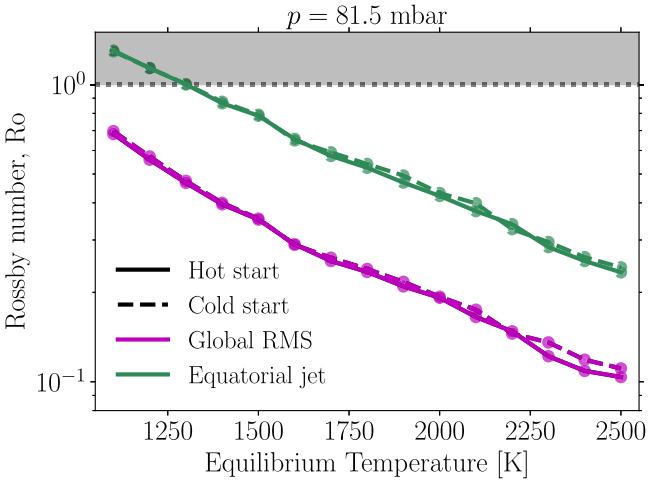

Figure 8. Rossby number numerically calculated from the GCM simulations in Suite 2. Solid lines connecting dots correspond to the simulations initialized with a hot start, while dashed lines correspond to the cold start cases. The green curves correspond to numerical estimates of the Rossby number using the zonal-mean zonal wind speed averaged within 10° of the equator, while the magenta curves correspond to numerical estimates using the global rms wind speed. The dotted horizontal line displays Ro = 1, which as shown in Equation (5) is approximately equivalent to the point where $\lambda_\beta/a = 1$ given that Ro $\approx (\lambda_\beta/a)^2$. The gray shaded region above the Ro = 1 line corresponds to the regime where the Rossby number and as a result the Rhines scale are large (i.e., the intermediate rotator regime described in Section 2.3). I find that when using the equatorial jet speed as the characteristic wind scale, GCM simulations of hot Jupiters can lie in the intermediate rotation regime for $T_{\rm eq} \lesssim 1300$ K, as expected from the scaling theory presented in Section 2.

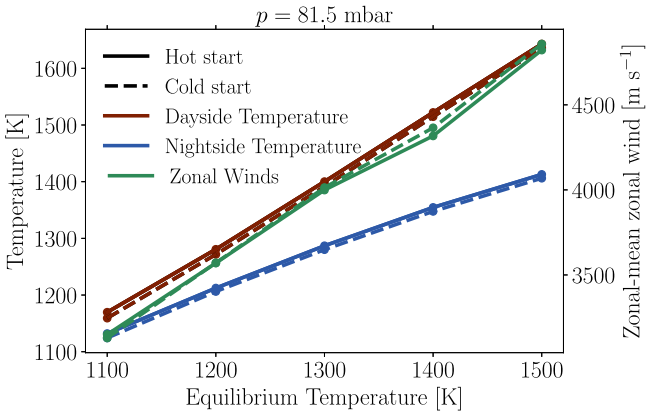

Figure 9. Dayside and nightside temperature as well as zonal-mean zonal wind speed at 81.5 mbar pressure as a function of equilibrium temperature from hot start cases (solid lines) and cold start cases (dashed lines) from the subset of cases in Suite 2(a). The dayside and nightside temperatures are averaged over the entire hemisphere, while the zonal-mean zonal wind is averaged within 10° of the equator. While the temperatures in the hot start models are slightly higher than those in the cold start models due to the long radiative adjustment timescale of hot-Jupiter atmospheres, I find no evidence for hysteresis in the averaged temperature or equatorial winds.

Jupiters undergo quasi-quadrennial oscillation-like stratospheric oscillations, as have been found in simulations of brown dwarfs and Jupiter with high vertical resolution (A. Showman et al. 2019; Y. Lian et al. 2023). Notably, simulations of temperate tidally locked planets exhibit quasi-biennial oscillation-like longitudinally asymmetric stratospheric oscillations (M. Cohen et al. 2022), which could have a potential analog in tidally locked gas giant simulations.

The impact of interior cooling on the deep atmospheric circulation was neglected in this work—notably, in all cases with double-gray radiative transfer, the intrinsic temperature $T_{\rm int}$ (corresponding to the net thermal flux) was fixed to 100 K. Previous work by L. Carone et al. (2020) found that the deep atmosphere can couple to the shallow atmosphere and drive subrotation on WASP-43b. In addition, H. Wang & R. Wordsworth (2020) studied the atmospheric circulations of sub-Neptunes with thick atmospheres and found that their deep circulation could exhibit regime transitions in the dynamics over timescales of tens of thousands of days. Importantly, the interior evolution of hot Jupiters is strongly time-dependent, with deep heating applied over evolutionary timescales required to explain both the present-day radii of hot Jupiters (D. Thorngren & J. Fortney 2018; P. Sarkis et al. 2021) as well as their reinflation during the main-sequence lifetimes of their host stars (D. Thorngren et al. 2021). As a result, the varying internal heat flux of hot Jupiters over time likely impacts their atmospheric circulation via the impact of interior heating on the three-dimensional radiative-convective boundary location (D. Thorngren et al. 2019; X. Zhang et al. 2023). Future work is required to study whether regime transitions in the atmospheric dynamics of hot Jupiters can occur as a function of interior heat flux.

A variety of other model effects could also potentially lead to hysteresis in either the atmospheric chemistry or the climate state, for instance including disequilibrium chemistry via vertical and horizontal quenching (C. Cooper & A. Showman 2006; B. Drummond et al. 2018b, 2020; M. Steinrueck et al. 2019; M. Zamyatina et al. 2023), aerosol (cloud and haze) radiative feedback (D. Christie et al. 2021; V. Parmentier et al. 2021; M. Roman et al. 2021; M. Steinrueck et al. 2021), and molecular hydrogen dissociation and recombination (T. Bell & N. Cowan 2018; X. Tan & T. Komacek 2019; A. Roth et al. 2021). All of these relevant processes are not included here for simplicity, because instead in this work I have focused only on hysteresis driven by the dry dynamics. Importantly, the bistability found in the TRAPPIST-1e simulations of D. Sergeev et al. (2022) may be driven by moisture and the resulting impact of latent heating on the dynamics. Given that including hydrogen dissociation and recombination is analogous to including moisture (albeit in a nondilute limit, T. Bell & N. Cowan 2018; X. Tan & T. Komacek 2019), it may be possible for ultra-hot Jupiters with high dayside atomic hydrogen mixing ratios to exhibit a dynamical bistability with regard to initial conditions. As a result, future work extending this study to the ultra-hot-Jupiter regime in simulations that include the thermochemical effects of molecular hydrogen dissociation and recombination is required to determine the level to which molecular hydrogen dissociation and recombination can cause the atmospheric circulation of ultra-hot Jupiters to exhibit a dependence on initial conditions.

6.2. Outlook

The results presented here imply that the atmospheric circulation of hot Jupiters may exhibit a limited dependence on initial thermal forcing and wind profiles, in broad agreement with the broad similarity of results from hot-Jupiter GCMs in the literature (K. Heng & A. Showman 2015; A. Showman et al. 2020). This implies that a wide range of GCM models will likely enable similar interpretation of observed phase curves and emission spectra. These results further imply that population-level studies of hot Jupiters should be robust to large differences in thermal structure for a given set of

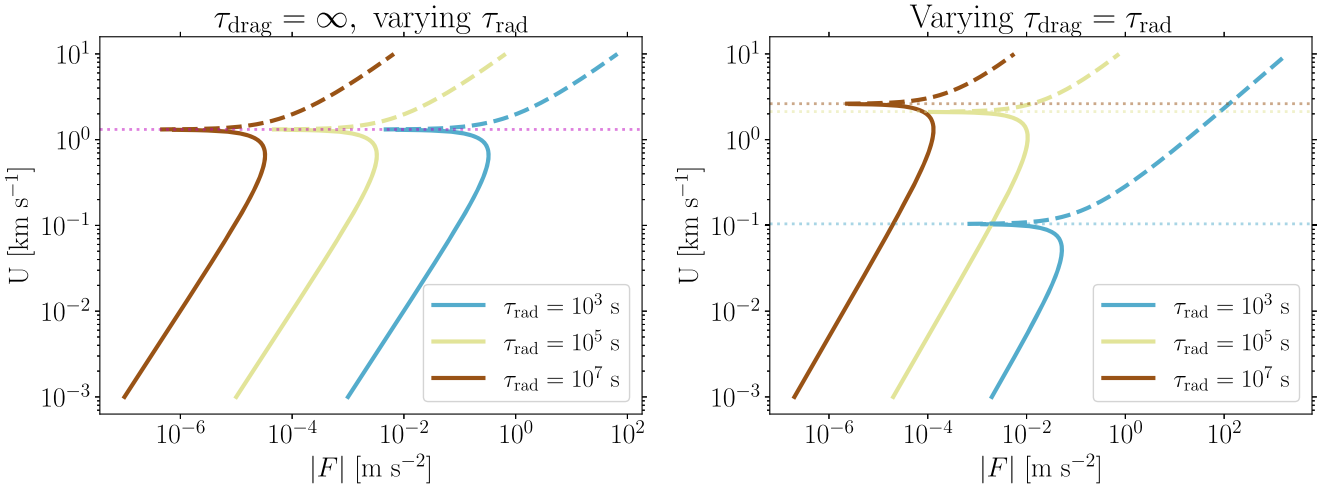

Figure 10. Relationship between the applied forcing F and characteristic horizontal wind speed U from Equation (13) for cases with varying radiative timescale and no frictional drag ($\tau_{\rm drag} = \infty$, left-hand side) and applied frictional drag with $\tau_{\rm drag} = \tau_{\rm rad}$ (right-hand side). Planetary parameters correspond to the equator of HD 209458b. Colors correspond to varying radiative timescales. Solid lines correspond to positive values of F and dashed lines correspond to negative values of F. Dotted horizontal lines display the equilibrium value of the characteristic wind speed (in the left-hand plot, this value is the same for all $\tau_{\rm rad}$). I find that the forcing is positive at wind speeds below where F has a minimum and negative at wind speeds above the minimum in F, implying that the horizontal winds only have one characteristic value at equilibrium for a given set of planetary parameters and combination of $\tau_{\rm drag}$ and $\tau_{\rm rad}$.

planetary properties (e.g., equilibrium temperature, metallicity, and gravity). The findings here also agree with the prediction of limited (but still potentially detectable) time-variability due to the lack of time-dependent transitions between model states (E. Rauscher et al. 2007; I. Dobbs-Dixon et al. 2010; T. Komacek & A. Showman 2016), which to date has been borne out in repeated Spitzer observations of hot-Jupiter secondary eclipses and phase curves (E. Agol et al. 2010; B. Kilpatrick et al. 2020; M. M. Murphy et al. 2023).

Though there is qualitative agreement between many hot-Jupiter modeling frameworks, there may still be important quantitative differences between model predictions. In this work, I only presented results from one model framework, using the MITgcm. There is a clear need to conduct model intercomparisons for hot Jupiters, as has been done previously for temperate terrestrial planets (J. Yang et al. 2016, 2019; T. J. Fauchez et al. 2022; D. E. Sergeev et al. 2022; M. Turbet et al. 2022). Such an intercomparison is currently being conducted through the Modeling the Circulation of Hot Exoplanet Atmospheres (MOCHA, led by N. Iro) exercise in the CUISINES framework (T. J. Fauchez et al. 2020). Intercomparisons such as MOCHA are required in order to determine the extent to which the conclusions presented in this work are valid in general, and to more broadly assess model agreement in the current era of JWST and improved high spectral resolution ground-based observations.

7. Conclusions

In this work, I study the potential for a dependence of the atmospheric circulation of hot Jupiters on initial conditions, especially at dynamical regime boundaries where such hysteresis has been found in previous exoplanet atmospheric circulation models. To do so, I conduct two separate suites of GCM simulations, one varying the initial wind structure and one varying the initial temperature profile. Both of these suites of simulations show no significant dependence on initial conditions, implying that the atmospheric circulation of typical hot Jupiters may exhibit limited hysteresis. I summarize my findings as follows:

1. The suite of three-dimensional GCMs of hot-Jupiter atmospheres with varying initial wind profile and basal drag strength show no strong dependence on their initial wind profile for both basal drag strengths considered. This result confirms the findings from the shallow-water models and three-dimensional GCMs of B. Liu & A. Showman (2013), and extends them to cases with weaker basal drag strength and long model runtimes of ~25,000 Earth days.
2. Hot Jupiters are expected from scaling arguments to potentially undergo a transition from intermediate rotators, where the Rossby deformation radius is smaller than the planetary radius but the Rhines scale is larger than the planetary radius, to rapid rotators, where both length scales are smaller than the planetary radius, with increasing instellation for a given host star type. Simulations of temperate rocky planets at another dynamical regime transition from intermediate to fast rotation have found a dependence of the resulting jet structure on the initial conditions (D. Sergeev et al. 2022). However, the hot-Jupiter GCMs presented here display no transition in the circulation regime or clear hysteresis at this theoretically predicted regime boundary with varying initial temperature profile, unlike in the case of temperate rocky planets.
3. These numerical results are interpreted in the context of a simple scaling theory leveraging the work of D. Perez-Becker & A. Showman (2013). This theory demonstrates that that the characteristic horizontal day-to-night wind speed has a single equilibrium value as a function of the planetary-scale forcing of hot Jupiters, implying that the strong day-to-night forcing of hot Jupiters drives the insensitivity to initial conditions in numerical simulations. Though the atmospheric circulation of hot Jupiters displays at most limited hysteresis, hysteresis in the dynamics of temperate rocky planets and

sub-Neptunes may be more likely due to the weaker large-scale forcing and the combination of day-to-night and equator-to-pole forcing contrasts that drives their circulation.

Acknowledgments

T.D.K. thanks the referee Neil Lewis for providing a deeply insightful review that significantly improved this manuscript. T.D.K. thanks Denis Sergeev, Jacob Haqq-Misra, and Arjun Savel for helpful comments on an early draft of this manuscript. T.D.K. also thanks Neil Lewis for insightful discussions on the utility of the Rhines Scale for tidally locked planets at Exoclimes VI. T.D.K. thanks Tiffany Kataria for guidance on setting up the MITgcm with varying initial wind profiles. T.D.K. acknowledges the University of Maryland supercomputing resources (http://hpcc.umd.edu) made available for conducting the research reported in this paper. The simulations with varying initial wind profiles were conducted on institutional computing resources at the University of Arizona Lunar and Planetary Laboratory, in collaboration with Adam Showman. T.D.K. further thanks Adam Showman for helpful discussions on the emergence of super-rotation.

ORCID iDs

Thaddeus D. Komacek https://orcid.org/0000-0002-9258-5311

References

Adcroft, A., Hill, C., Campin, J., Marshall, J., & Heimbach, P. 2004, MWRv, 132, 2845
Agol, E., Cowan, N., Knutson, H., et al. 2010, ApJ, 721, 1861
Batygin, K., Stanley, S., & Stevenson, D. 2013, ApJ, 776, 53
Bell, T., & Cowan, N. 2018, ApJL, 857, L20
Bell, T. J., Crouzet, N., Cubillos, P. E., et al. 2024, NatAs, 8, 879
Bell, T. J., Dang, L., Cowan, N. B., et al. 2021, MNRAS, 504, 3316
Beltz, H., Rauscher, E., Roman, M., & Guilliat, A. 2022, AJ, 163, 35
Berardo, D., Cumming, A., & Marleau, G. 2017, ApJ, 834, 149
Carone, L., Baeyens, R., Mollière, P., et al. 2020, MNRAS, 496, 3582
Challener, R. C., & Rauscher, E. 2022, AJ, 163, 117
Checlair, J. H., Olson, S. L., Jansen, M. F., & Abbot, D. S. 2019, ApJL, 884, L46
Cho, J., Polichtchouk, I., & Thrastarson, H. 2015, MNRAS, 454, 3423
Cho, J., Skinner, J., & Thrastarson, H. 2021, ApJL, 913, L32
Christie, D., Mayne, N., Lines, S., et al. 2021, MNRAS, 506, 4500
Christie, D., Mayne, N., Zamyatina, M., et al. 2024, MNRAS, 532, 3001
Cohen, M., Bollasina, M. A., Palmer, P. I., et al. 2022, ApJ, 930, 152
Cooper, C., & Showman, A. 2006, ApJ, 649, 1048
Coulombe, L.-P., Benneke, B., Challener, R., et al. 2023, Natur, 620, 292
Dang, L., Cowan, N., Schwartz, J., et al. 2018, NatAs, 2, 220
Dobbs-Dixon, I., & Agol, E. 2013, MNRAS, 435, 3159
Dobbs-Dixon, I., Cumming, A., & Lin, D. 2010, ApJ, 710, 1395
Drummond, B., Hebrard, E., Mayne, N., et al. 2020, A&A, 636, A68
Drummond, B., Mayne, N., Manners, J., et al. 2018a, ApJL, 855, L31
Drummond, B., Mayne, N., Manners, J., et al. 2018b, ApJ, 869, 28
Fauchez, T. J., Turbet, M., Wolf, E. T., et al. 2020, GMD, 13, 707
Fauchez, T. J., Villanueva, G. L., Sergeev, D. E., et al. 2022, PSJ, 3, 213
Guillot, T., Burrows, A., Hubbard, W., Lunine, J., & Saumon, D. 1996, ApJL, 459, L35
Hammond, M., & Abbot, D. 2022, MNRAS, 511, 2313
Hammond, M., Bell, T. J., Challener, R. C., et al. 2024, AJ, 168, 4
Hammond, M., & Lewis, N. 2021, PNAS, 118, 2022705118
Hammond, M., & Pierrehumbert, R. 2018, ApJ, 869, 65
Hammond, M., Tsai, S.-M., & Pierrehumbert, R. T. 2020, ApJ, 901, 78
Haqq-Misra, J., Wolf, E., Joshi, M., Zhang, X., & Kopparapu, R. 2018, ApJ, 852, 67
Heng, K., Menou, K., & Phillips, P. 2011, MNRAS, 413, 2380
Heng, K., & Showman, A. 2015, AREPS, 43, 509
Iro, N., Bézard, B., & Guillot, T. 2005, A&A, 436, 719
Kataria, T., Showman, A., Fortney, J., et al. 2015, ApJ, 801, 86
Kempton, E., & Rauscher, E. 2012, ApJ, 751, 117
Kilpatrick, B., Kataria, T., Lewis, N., et al. 2020, AJ, 159, 51
Koll, D., & Komacek, T. 2018, ApJ, 853, 133
Komacek, T., & Showman, A. 2016, ApJ, 821, 16
Komacek, T., & Showman, A. 2020, ApJ, 888, 2
Komacek, T., Showman, A., & Tan, X. 2017, ApJ, 835, 198
Komacek, T., & Tan, X. 2018, RNAAS, 2, 36
Kylling, A., & Stamnes, K. 1992, JCoPh, 102, 265
Laughlin, G., Crismani, M., & Adams, F. 2011, ApJL, 729, L7
Lee, E., Parmentier, V., Hammond, M., et al. 2021, MNRAS, 506, 2695
Lewis, N., & Hammond, M. 2022, ApJ, 941, 171
Lian, Y., Tan, X., & Hu, Y. 2023, ApJ, 958, 50
Liu, B., & Showman, A. 2013, ApJ, 770, 42
Lothringer, J., Barman, T., & Koskinen, T. 2018, ApJ, 866, 27
Malsky, I., Rauscher, E., Roman, M. T., et al. 2024, ApJ, 961, 66
Mansfield, M., Schlawin, E., Lustig-Yaeger, J., et al. 2020, MNRAS, 499, 5151
May, E. M., Stevenson, K. B., Bean, J. L., et al. 2022, AJ, 163, 256
Mendonça, J. M. 2019, MNRAS, 491, 1456
Mikal-Evans, T., Sing, D., Dong, J., et al. 2023, ApJL, 943, L17
Murphy, M. M., Beatty, T. G., Roman, M. T., et al. 2023, AJ, 165, 107
Noda, S., Ishiwatari, M., Nakajima, K., et al. 2017, Icar, 282, 1
Parmentier, V., Showman, A., & Fortney, J. 2021, MNRAS, 501, 78
Perez-Becker, D., & Showman, A. 2013, ApJ, 776, 134
Perna, R., Menou, K., & Rauscher, E. 2010, ApJ, 719, 1421
Pierrehumbert, R., & Hammond, M. 2019, AnRFM, 51, 275
Rauscher, E., & Kempton, E. M. R. 2014, ApJ, 790, 79
Rauscher, E., & Menou, K. 2013, ApJ, 764, 103
Rauscher, E., Menou, K., Cho, J. Y.-K., Seager, S., & Hansen, B. M. S. 2007, ApJL, 662, L115
Rhines, P. 1975, JFM, 69, 417
Rogers, T. 2017, NatAs, 1, 131
Rogers, T., & Showman, A. 2014, ApJL, 782, L4
Roman, M., Kempton, E., Rauscher, E., et al. 2021, ApJ, 908, 101
Roth, A., Drummond, B., Hebrard, E., et al. 2021, MNRAS, 505, 4515
Roth, A., Parmentier, V., & Hammond, M. 2024, MNRAS, 531, 1056
Sarkis, P., Mordasini, C., Henning, T., Marleau, G., & Molliére, P. 2021, A&A, 645, A79
Schneider, A., Carone, L., Decin, L., et al. 2022, A&A, 664, A56
Schubert, G., & Mitchell, J. 2013, in Comparative Climatology of Terrestrial Planets, ed. S. Mackwell et al. (Tucson, AZ: Univ. Arizona Press)
Sergeev, D., Lewis, N., Lambert, F., et al. 2022, PSJ, 3, 214
Sergeev, D. E., Fauchez, T. J., Turbet, M., et al. 2022, PSJ, 3, 212
Shell, K., & Held, I. 2004, JAtS, 61, 2928
Showman, A., Cho, J., & Menou, K. 2010, in Exoplanets, ed. S. Seager (Tucson, AZ: Univ. Arizona Press)
Showman, A., Fortney, J., Lewis, N., & Shabram, M. 2013, ApJ, 762, 24
Showman, A., & Guillot, T. 2002, A&A, 385, 166
Showman, A., Lewis, N., & Fortney, J. 2015, ApJ, 801, 95
Showman, A., & Polvani, L. 2010, GeoRL, 37, L18811
Showman, A., & Polvani, L. 2011, ApJ, 738, 71
Showman, A., Tan, X., & Parmentier, V. 2020, SSRv, 216, 139
Showman, A., Tan, X., & Zhang, X. 2019, ApJ, 883, 4
Skinner, J. W., & Cho, J. Y. K. 2021, MNRAS, 504, 5172
Skinner, J. W., & Cho, J. Y. K. 2022, MNRAS, 511, 3584
Stamnes, K., Tsay, S., Wiscombe, W., & Jayaweera, K. 1988, ApOpt, 27, 2502
Steinrueck, M., Parmentier, V., Showman, A., Lothringer, J., & Lupu, R. 2019, ApJ, 880, 14
Steinrueck, M., Showman, A., Lavvas, P., et al. 2021, MNRAS, 504, 2783
Tan, X., & Komacek, T. 2019, ApJ, 886, 26
Tan, X., Komacek, T. D., Batalha, N. E., et al. 2024, MNRAS, 528, 1016
Thorngren, D., & Fortney, J. 2018, AJ, 155, 214
Thorngren, D., Fortney, J., Lopez, E., Berger, T., & Huber, D. 2021, ApJL, 909, L16
Thorngren, D., Gao, P., & Fortney, J. 2019, ApJL, 884, L6
Tsai, S., Dobbs-Dixon, I., & Gu, P. 2014, ApJ, 793, 141
Turbet, M., Bolmont, E., Chaverot, G., et al. 2021, Natur, 598, 276
Turbet, M., Fauchez, T. J., Sergeev, D. E., et al. 2022, PSJ, 3, 211
Wang, H., & Wordsworth, R. 2020, ApJ, 891, 7
Wang, Y., Read, P., Tabataba-Vakili, F., & Young, R. 2018, QJRMS, 144, 2537
Yang, J., Leconte, J., Wolf, E. T., et al. 2016, ApJ, 826, 222
Yang, J., Leconte, J., Wolf, E. T., et al. 2019, ApJ, 875, 46
Youdin, A., & Zhu, Z. 2025, arXiv:2501.13214
Zamyatina, M., Hebrard, E., Drummond, B., et al. 2023, MNRAS, 519, 3129
Zhang, M., Knutson, H., Kataria, T., et al. 2018, AJ, 155, 83
Zhang, X. 2020, RAA, 20, 099
Zhang, X., Li, C., Ge, H., & Le, T. 2023, ApJ, 957, 22